Journal of Environmental Radioactivity 280 (2024) 107554

Contents lists available at ScienceDirect

Journal of Environmental Radioactivity

journal homepage: www.elsevier.com/locate/jenvrad

Integrated radiation air dose rate maps over the 80 km radius of the Fukushima Daiichi Nuclear Power Plant and the entire Fukushima Prefecture during 2011–2022

Kazuyuki Sakuma [a,b,*], Hiroshi Kurikami [a], Haruko Wainwright [b], Soichiro Tanimori [c], Fumiya Nagao [a], Kotaro Ochi [a], Yukihisa Sanada [a], Kimiaki Saito [d]

[a] Fukushima Research and Engineering Institute, Japan Atomic Energy Agency, Fukushima, 975-0036, Japan
[b] Department of Nuclear Science and Engineering, Massachusetts Institute of Technology, MA, 02139, USA
[c] AdvanceSoft Corporation, Tokyo, 101-0062, Japan
[d] Center for Computational Science & e-Systems, Japan Atomic Energy Agency, Chiba, 277-0871, Japan

ABSTRACT

In this study, we created integrated radiation air dose rate maps in the Fukushima region during 2011–2022 using airborne, car-borne, and walk surveys and fixed-location measurements. We applied a Bayesian geostatistical method to the 80 km radius of the Fukushima Daiichi Nuclear Power Plant and the entire Fukushima Prefecture while considering the history of the evacuation zone lifting in Fukushima. The integrated maps in this study fixed the bias to underestimate the air dose rates in forest areas and created integrated maps with a wider area and time series than previous studies. Furthermore, the results improved our understanding of the spatial heterogeneity of air dose rates. The correlations between walk and airborne surveys and walk and car-borne surveys changed over time (the walk survey includes fixed-location measurements), with the decreasing rates of air dose rate being faster for car-borne surveys, walk surveys, fixed-location measurements, and airborne surveys, in that order. The temporal changes in the variograms indicate that the heterogeneity of the radiocesium distribution in the environment varies with time due to decontamination activities and weathering effects. The trends inside and outside the evacuation zone differ. The temporal changes in the air dose rates from the integrated maps show a decrease between fixed-location measurements and the airborne survey. This decreasing rate mostly reflects the overall decrease in air dose rates. The results of this study could be used to evaluate detailed exposure doses to the public.

1. Introduction

After the Fukushima Daiichi Nuclear Power Plant (FDNPP) accident, several radionuclides were deposited in the environment. In particular, radiocesium (^{134}Cs and ^{137}Cs), which emits gamma rays, is the most critical element for considering the medium-to long-term external exposure to humans due to their long half-lives (2.06 y for ^{134}Cs and 30.1 y for ^{137}Cs) and the total amount of deposition to the terrestrial area (approximately 2.65 PBq for ^{137} Cs; Kato et al., 2019). A detailed map of the ambient dose equivalent rates (referred to as air dose rate hereafter) derived from radiocesium for the entire Fukushima Prefecture is significant in estimating human exposure from the post-accident period to the present more precisely.

After the FDNPP accident, various organizations have made considerable efforts to monitor the air dose rates. The mapping project started in 2011 b y the Japan Atomic Energy Agency (JAEA) supported by the national government to quantify the radiological conditions in detail for a broad area in Fukushima Prefecture and other prefectures contaminated by radionuclides (Saito and Onda, 2015). This project was conducted to measure the air dose rates using several methods from the initial periods to the present intermittently: fixed-location measurements with NaI(Tl) survey meters (Mikami et al., 2015a, 2019), car-borne survey (Andoh et al., 2015, 2018a), walk survey (Andoh et al., 2015; Andoh et al., 2018b) and unmanned helicopter survey (Sanada et al., 2018). Extensive airborne surveys have been implemented in another project (Sanada et al., 2014, 2018). Also, local and national governments have continuously monitored the air dose rates using monitoring posts (Fukushima Prefecture, 2022) and fixed-location measurements in the forests yearly (MAFF, 2022).

The measurement methods above are described below. An airborne survey can broadly and quickly estimate the air dose rate 1 m above the ground. However, the flight characteristics 300 m above the ground and the conversion of its count per second to the air dose rate at 1 m from the ground result in a mean air dose rate value in a large area. This causes significant uncertainties about the air dose rate at 1 m from the ground measured by airborne survey (Sanada et al., 2014, 2018). A previous

* Corresponding author. Fukushima Research and Engineering Institute, Japan Atomic Energy Agency, Fukushima, 975-0036, Japan.
E-mail address: sakuma.kazuyuki@jaea.go.jp (K. Sakuma).

https://doi.org/10.1016/j.jenvrad.2024.107554
Received 3 July 2024; Received in revised form 15 October 2024; Accepted 16 October 2024
Available online 19 October 2024
0265-931X/© 2024 The Authors. Published by Elsevier Ltd. This is an open access article under the CC BY license (http://creativecommons.org/licenses/by/4.0/).

Table 1
Air dose rate datasets for integrated maps.

FY	Date of decay correction (MM/DD/YYYY)	Air-borne survey	Car-borne survey	Walk survey	Measurement at a fixed location
2011	February 7, 2011	JAEA (May–July)	JAEA (June), TEPCO (Aug)	–	JAEA (June–July) FP (Aug–Sept) MAFF (July) CAO&MEXT (June)
2012	6/28/2012	JAEA (June)	JAEA (Aug–Oct), TEPCO (July)	–	JAEA (Aug–Sept) FP (May–June) MAFF (July)
2013	9/28/2013	JAEA (Aug–Sept)	JAEA (June–Aug), TEPCO (Nov)	JAEA (June, Nov)	JAEA (Oct–Dec) FP (May–June) MAFF (July)
2014	July 11, 2014	JAEA (Sept–Nov)	JAEA (Nov–Dec), TEPCO (Oct)	JAEA (July, Oct)	JAEA (Nov–Dec) FP (May–June) MAFF (June–Jan)
2015	April 11, 2015	JAEA (Sept–Nov)	JAEA (Nov–Dec), TEPCO (Nov)	JAEA (June, Oct)	JAEA (Aug–Sept) FP (May–June) MAFF (June–Jan)
2016	11/18/2016	JAEA (Sept–Nov)	JAEA (Oct–Dec), TEPCO (Nov)	JAEA (June, Oct)	JAEA (Aug–Oct) FP (May–July) MAFF (June–Dec)
2017	11/16/2017	JAEA (Sept–Nov)	JAEA (Oct), TEPCO (Oct)	JAEA (Oct)	JAEA (Aug–Oct) FP (Apr–July) MAFF (June–Feb)
2018	11/15/2018	JAEA (Nov)	JAEA (Nov), TEPCO (Oct)	JAEA (Nov)	JAEA (Sept–Oct) FP (Apr–July) MAFF (June–Jan)
2019	February 11, 2019	JAEA (Nov)	JAEA (Nov), TEPCO (Oct)	JAEA (Oct)	JAEA (Aug–Sept) FP (Apr–July) MAFF (June–Dec)
2020	10/30/2020	JAEA (Oct)	JAEA (Nov), TEPCO (Oct)	JAEA (Oct)	JAEA (Aug–Oct) FP (Apr–Aug) MAFF (June–Nov)
2021	10/25/2021	JAEA (Oct)	JAEA (Nov), TEPCO (Nov)	JAEA (Oct)	JAEA (Aug–Sept) FP (Apr–July) MAFF (July–Dec)
2022	10/30/2022	JAEA (Oct)	JAEA (Nov), TEPCO (Nov)	JAEA (Oct)	JAEA (Aug–Oct) FP (Apr–May) MAFF (June–Nov)

JAEA: the data was taken by JAEA.
TEPCO: the data taken by TEPCO.
FP: the data was taken by Fukushima Prefecture.
MAFF: the data was taken by the Ministry of Agriculture, Forestry and Fisheries.
CAO&MEXT: the data was taken by the Cabinet Office, Government of Japan, and the Ministry of Education, Culture, Sports, Science and Technology.

study highlighted that airborne surveys tend to overestimate the air dose rate 1 m above the ground compared to ground observations (Wainwright et al., 2017, 2019). Furthermore, car-borne surveys can also broadly and quickly measure air dose rates along the road, but the measurement data are limited on the road; thus, the air dose rate could not reflect the actual living environment. However, a walk survey can measure air dose rates reflecting the actual living environment, although the targeted area is limited. Therefore, an air dose rate map based on a walk survey is likely to be desirable to estimate human exposure.

Wainwright et al. (2017) developed a method to estimate the distribution of air dose rate equivalent to a walk survey by integrating three scale and resolution datasets and demonstrated its effectiveness for Fukushima City. In this method, the prior distribution is estimated using the geostatistics processing of walk surveys, and then, the posterior distribution is estimated using Bayesian updating with car-borne and airborne survey data. The walk survey data is considered the true value because it is close to the living environment. Car-borne and airborne survey data are used to improve accuracy over a wide area. It combines the advantages of highly accurate walk surveys and the wide-area measurement capability of car-borne and airborne surveys. Furthermore, Wainwright et al. (2019) expanded the applied area and showed the temporal changes in the air dose rate maps during 2014–2016 within the evacuation area and predictions of the air dose rate map for 2026.

However, significant challenges exist in creating air dose rate maps. One is that the previous approaches (Wainwright et al., 2017, 2019) could not create integrated maps in 2011 and 2012 and over the 80 km radius from the FDNPP because walk survey data were not measured. The other is that walk survey data were measured in limited areas where people only walk; thus, the data only cover part of the area spatially; for example, it was not measured at agricultural fields, school yards, parks, and campsites. Forest locations far from roads tend to have higher air dose rates than those near a road (radiocesium on roads tends to be washed off by rainfall, but tends to stay in surface soil and forest litter in forests); therefore, the air dose rate in forests is underestimated on the integrated maps created before.

In this study, we expanded Wainwright et al.'s (2017, 2019) method on a larger scale using a domain decomposition method. We also expanded the data by treating fixed-location measurements, including forest areas, as a walk survey and created more accurate air dose rate maps for a larger area each year from 2011 to 2022. The maps produced in this study can be used to reassess post-accident exposure doses and evaluate trends in air dose rates over time as representative dose rate maps that combine the high accuracy of walk surveys and the spatial coverage of car-borne and airborne surveys.

2. Methods

The study area includes the 80 km radius of the FDNPP and the entire Fukushima Prefecture.

2.1. Data description

In this study, we used four air dose rate datasets from 2011 to 2022: 1) airborne survey, 2) car-borne survey, 3) walk survey, and 4) fixed-location measurements. However, no walk survey data were measured for 2011–2012. Airborne survey data only cover an 80 km radius of the FDNPP for 2011–2013. As much as possible, each survey was measured at the same locations each year; however, a few additions and changes exist for various reasons each year. For example, the number of measurement locations in the vicinity of the FDNPP for walk surveys has increased since 2014. Table 1 summarizes the data. The data are published in the Database for Radioactive Substance Monitoring Data (EMDB) at the JAEA (https://emdb.jaea.go.jp/emdb/). The comparison of air dose rates from the four surveys is shown by Sanada et al. (2019).

Airborne surveys can obtain air dose rate maps 1 m above the ground by flights of 300 m from the ground. The airborne surveys employed a

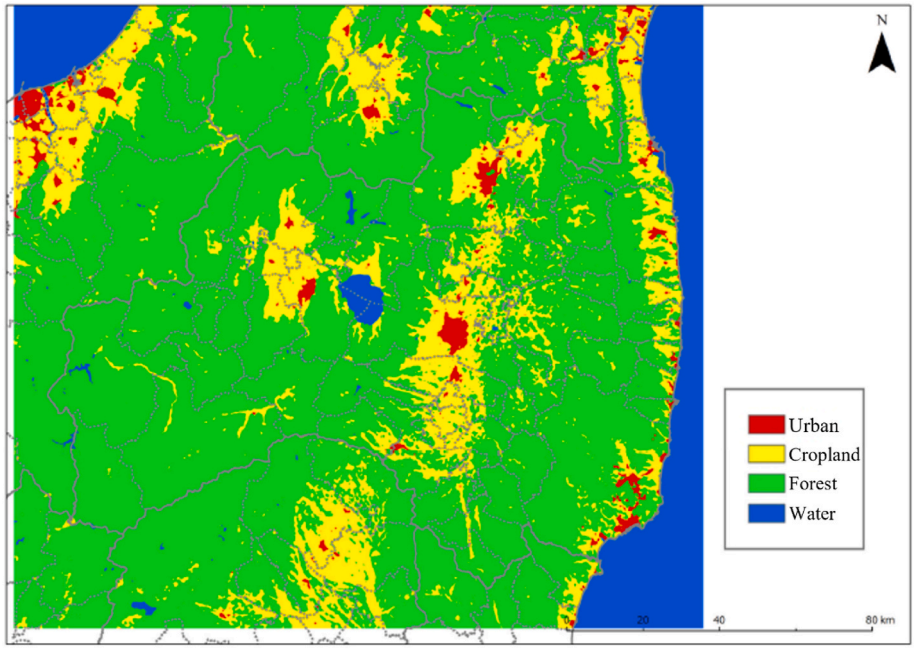

Fig. 1. Land-use distribution after smoothing over Fukushima Prefecture. The ALOS21.11 (JAXA, 2022) was used for the map; the map was created by ArcGIS (ESRI Japan).

large NaI(Tl) detector with high detection efficiency attached inside a helicopter. (Sanada et al., 2014, 2018). The count rate measured was converted to the air dose rate 1 m above the ground using a calibration factor determined in a calibration test performed in actual fields (Sanada et al., 2014). The datasets were provided within a 250 m × 250 m mesh after interpolation using the inverse distance weighting method (Wong, 2017). The JAEA collected the data.

Car-borne surveys can obtain air dose rate maps along the road. The JAEA (Andoh et al., 2015, 2018a) and Tokyo Electric Power Company (TEPCO) (METI, 2022) collected the data used in this study, each using different measurement systems. The JAEA used the Kyoto University RAdiation MApping (KURAMA)-II system (Tanigaki et al., 2015) mounted on a car. The system included a CsI(Tl) scintillation detector, the Global Positioning System, and a software-designed control device (Tsuda et al., 2015). The air dose rates and coordinates were measured every 3 s while the car moved. The datasets were averaged within the 100 m × 100 m mesh. However, TEPCO used a NaI(TI) and an ionization chamber-type survey meter mounted on a car.

The JAEA collected the walk survey data using the KURAMA-II system in various human living environments (Andoh et al., 2018b) within an 80 km area from the FDNPP. In these surveys, a person carrying the KURAMA-II system walked around a 1 × 1 km^2 area, and approximately 600 areas were targeted in each campaign. The walk survey data were primarily collected from publicly accessible regions, such as pedestrian paths along roads. The datasets were averaged within the 20 m × 20 m mesh. The data we used from 2013 to 2016 were measured twice a year.

The JAEA, Fukushima Prefecture, and the Ministry of Agriculture Forestry and Fisheries MAFF (2022) collected the fixed-location measurements. The JAEA selected undisturbed fields where neither human disturbance nor high flooding were expected to change the field conditions (Mikami et al., 2015b, 2019). The number of measurement locations was approximately 6500 per year. The air dose rates were measured using a NaI(Tl) survey meter. For the Fukushima Prefecture measurement (Fukushima Prefecture, 2022), a 1 × 1 km^2 area was divided into a 100 m mesh, and the air dose rates were measured 1 m above the ground surface on roads or public facilities. The MAFF (MAFF, 2022) selected approximately 200 sites in the forest for trails and trailheads in national forests in Fukushima Prefecture. The air dose rates were measured 1 m above the ground.

2.2. Methodology

2.2.1. Theory

We used the data integration methodology developed by Wainwright et al. (2017). This method uses geostatistics to represent spatial heterogeneous structures and Bayesian hierarchical models to consistently integrate multiscale, multitype datasets. We denote the air dose rate at the ith pixel by y_i, where $i = 1, \ldots, n$. We also denote three datasets by three vectors, representing the airborne survey data $\mathbf{z_A}$ (each data point is represented by $\mathbf{z}_{\mathbf{A},j}$, where $j = 1, \ldots, m_A$), car-borne survey data $\mathbf{z_C}$ (each data point is represented by $\mathbf{z}_{\mathbf{C},j}$, where $j = 1, \ldots, m_C$), and walk survey and fixed-location measurement data (each data point is represented by $\mathbf{z}_{\mathbf{W},j}$, where $j = 1, \ldots, m_W$). The goal is to estimate the posterior distribution of the air dose rate map $\mathbf{y}$ (i.e., the vector representing the air dose rates at all the pixels) conditioned on these three datasets ($\mathbf{z_A}$, $\mathbf{z_C}$, and $\mathbf{z_W}$) written as $p(\mathbf{y} \mid \mathbf{z_A}, \mathbf{z_C}, \mathbf{z_W})$. By applying Bayes' rule, we can rewrite this posterior distribution as

$$p(\mathbf{y} \mid \mathbf{z_A}, \mathbf{z_C}, \mathbf{z_W}) \propto p(\mathbf{z_A} \mid \mathbf{y})\, p(\mathbf{z_C} \mid \mathbf{y})\, p(\mathbf{y} \mid \mathbf{z_W}), \tag{1}$$

We assume that the datasets are conditionally independent, given the air dose rate distribution $\mathbf{y}$. Wainwright et al. (2017) provide a detailed description.

2.2.2. Data preprocessing

We compared the air dose rates for each land use in this study because the features of air dose rates vary at different land-use types. The land use data by the Advanced Land Observing Satellite (ALOS) provided by the Japan Aerospace Exploration Agency (JAXA) (2022) (Fig. 1) was used. The data were updated once every few years; thus, we used ALOS 16.09, 18.03, and 21.03/21.11 for the integrated maps during 2011–2013, 2014–2017, and 2018–2022, respectively. A data smoothing method was used for land use because the ALOS resolution is too high to apply our developed method. Land use was reclassified into urban, cropland, forest, and water bodies, and the most frequent land use from the data in the 13 × 13 cells near the target cell was used as the

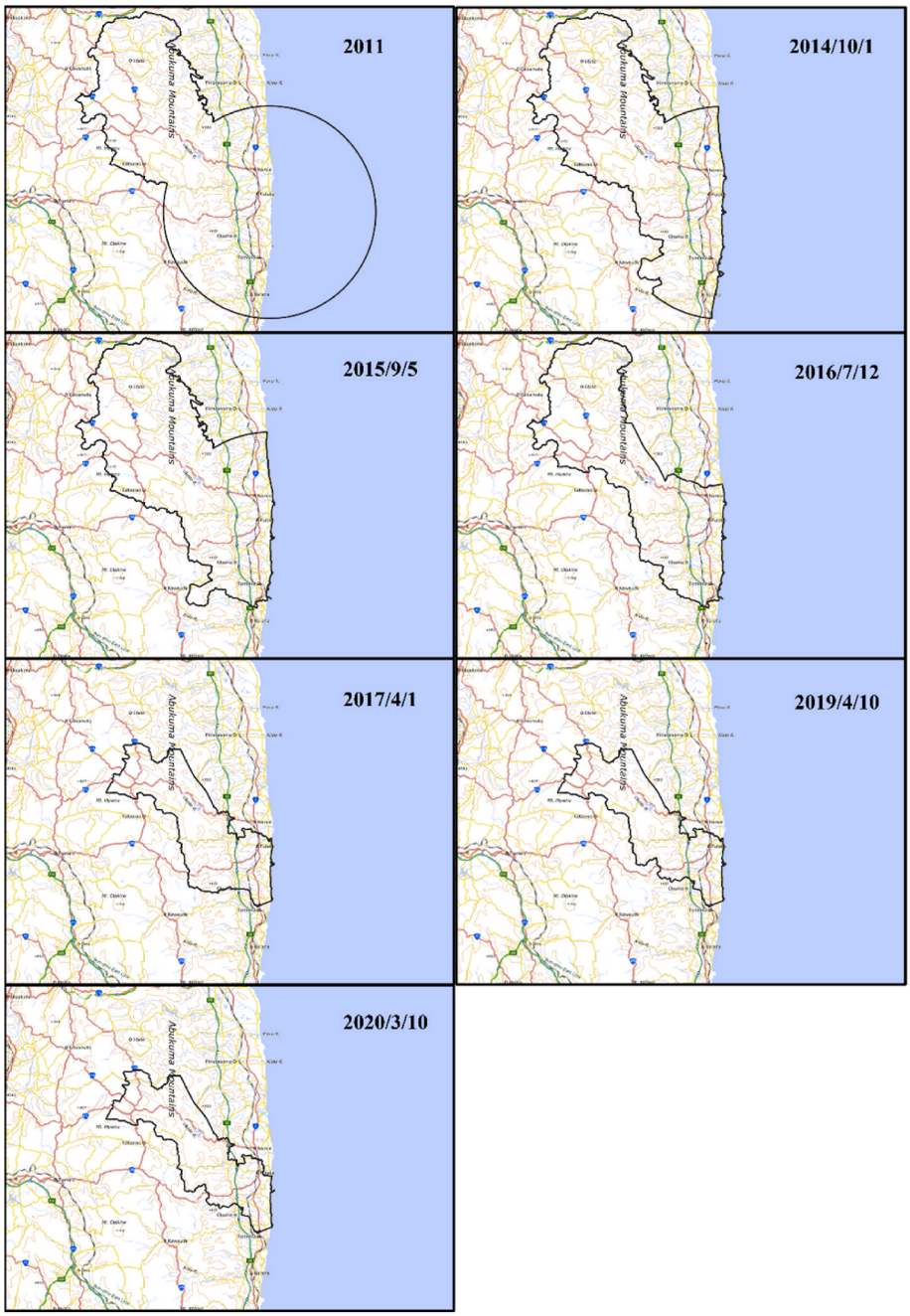

Fig. 2. The lifting history of the evacuation zone in Fukushima (dates in the figures are in the format year/month/day).

land use of the cell in question.

The air dose rate dataset values were corrected to consider the decay of ^{134}Cs and ^{137}Cs. The background effect from natural radionuclides was subtracted from the measured value during the correction, and the air dose rates were corrected. After the correction, the natural background effect was added back in. Data on fixed-location measurements were deleted when the distances between the walk survey and fixed-location measurement data were close (<20 m) to avoid divergence when determining the variogram parameters described in the following section.

We obtained the correlation coefficients between the airborne and walk surveys, and car-borne and walk surveys for each land use for each year (urban, cropland, and forest). The fixed-location measurements were considered equivalent to the walk survey. Walk survey data and fixed-location measurements within 200 m from the airborne survey data and 20 m from the car-borne survey data were used to calculate the correlation coefficients between the airborne and walk surveys and the car-borne and walk surveys, respectively. No walk survey data were available for 2011–2012; therefore, only fixed-location measurement data were used for 2011–2012 when we calculated the correlation coefficients.

Empirical variograms needed for the kriging method at each land use ($v_k(d)$) were created to spatially extrapolate the walk survey and fixed-location measurement air dose rates,

$$v_k(d) = \frac{1}{N_k} \sum_{i=1}^{N_k} \delta_{k,l_p} \delta_{k,l_q} \left[\mu_k(x_p) - \mu_k(x_q) \right]^2, \tag{2}$$

where d is the lag distance, k is the land use (urban, cropland, and forest), x_p and x_q are the coordinates of data points p and q, respectively

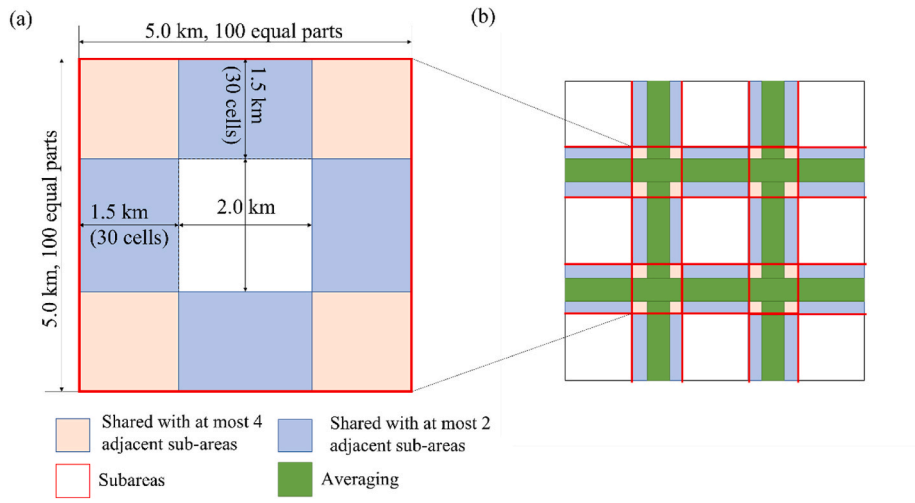

Fig. 3. Diagrams of the domain decomposition: (a) 5 km × 5 km subarea, (b) the areas where the averaging process was performed in a 5 km × 5 km subarea.

(UTM zone 54N of projected coordinate system was used), l_p and l_q are the land use at x_p and x_q, respectively, N_k is the number of data at land use k within lag distance d, and μ_k (x_p) and μ_k (x_q) are the common logarithms of air dose rates at land use k.

We used the standard variogram approach in the GeoR package of the statistical software R (Ribeiro and Diggle, 2001). An exponential model was used as a variogram model,

$$f_k(d) = n_k + s_k\left[1 - \exp\left(-\frac{d}{r_k}\right)\right], \tag{3}$$

where $f_k(d)$ is the variogram model for land use k, d is the lag distance, r_k is the range, s_k is the partial sill, and n_k is the nugget. Wainwright et al. (2017) provide a detailed description and the comparison with and without the Bayesian/Variogram approach can be found in Wainwright et al. (2019).

We also considered the changes in the evacuation zone to understand the changes in the air dose rates inside and outside the evacuation zone when we determined the variogram parameters. Fig. 2 shows the history of the lifting of the evacuation zone.

2.2.3. Data integration and estimation for air dose rate maps by domain decomposition

We introduced a method of dividing the whole area into subdomains and computing in parallel to Wainwright et al. (2017, 2019) for using many air dose rate datasets. In Fig. 3(a), a 5 km × 5 km subarea was created, with a 50 m grid (100 × 100) created within the area, overlapping the adjacent subareas by 1.5 km. The central 4 km^2 was not overlapped. The walk survey and fixed-location measurement data were averaged within each subarea because these data were not necessarily present when the area was divided. If no data existed within the subarea, the average included the cells around the subarea.

The air dose rates within the overlapping areas were averaged after integrating and estimating the data in parallel for each subarea. Fig. 3(b) shows that since the reliability of the simulated results is considered low in the periphery of the small area, it was not used for the averaging process. The averaging process was performed in the center of the overlapping area (green). Also, the data in the water body were deleted.

3. Results and discussion

3.1. Relationships between different surveys

Supplementary Figs. S1 and S2 show the relationships between the airborne and walk surveys, including fixed-location measurements, and the car-borne and walk surveys, including fixed-location measurements, for each land use (urban, cropland, and forest) for the area within an 80 km radius from the FDNPP and the entire Fukushima Prefecture during 2011–2022. The correlation coefficients for urban, cropland, and forest areas between the airborne and walk surveys were 0.81–0.98 (mean: 0.89), 0.91–0.97 (mean: 0.93), and 0.93–0.96 (mean: 0.95) and between the car-borne and walk surveys were 0.76–0.95 (mean: 0.83), 0.89–0.97 (mean: 0.93), and 0.90–0.98 (mean: 0.94). All results show a decreasing trend in air dose rates over the years while maintaining strong positive correlations. However, the urban areas show a faster decrease in air dose rates and greater variability compared to the cropland and forest areas.

Supplementary Fig. S3 shows the relationships between walk survey and fixed-location measurements from 2013 to 2020. Walk survey data within 50 m from fixed-location measurements were used to calculate their correlation coefficients. The relationship between the walk survey and fixed-location measurements in 2013 was 1.0:1.06, indicating that the integrated maps in 2011 and 2012 without walk survey data are reasonable. However, the air dose rate measured by walk surveys was lower than that measured by fixed-location measurements over the years because walk surveys were conducted along the road, and radiocesium on the roads tends to be washed off (Takeishi et al., 2017; Yoshimura et al., 2017). However, the air dose rates measured by the walk survey and fixed-location measurements in proximity to each other could be the same (Sato et al., 2019).

Supplementary Fig. S4 shows the relationships between the different surveys in 2011 and 2020. From Supplementary Fig. S4, the air dose rates measured by different surveys in 2011 were similar. In contrast, when the average air dose rates by the fixed-location measurements were set at 1 in 2020, the slope values of the relationships among airborne, walk, and car-borne surveys were approximately 1.3, 0.6, and 0.5, respectively. Therefore, the time series of the air dose rates measured by different surveys differed, possibly caused by radiocesium behavior in the local environment (for example, ^{137}Cs wash-off on asphalts and deeper migration in soil). Also, it could be related to the variogram changes mentioned in the following section.

The survey locations each year are also a factor impacting changes in both air dose rates and relationships between surveys. However, each survey was measured at the same locations each year as much as possible, the survey locations could have little impact on the analysis in this study.

3.2. Variogram changes

Supplementary Tables S1–S6 show the variogram parameters of the walk surveys for each land use during 2013–2022. Figs. 4 and 5 show the

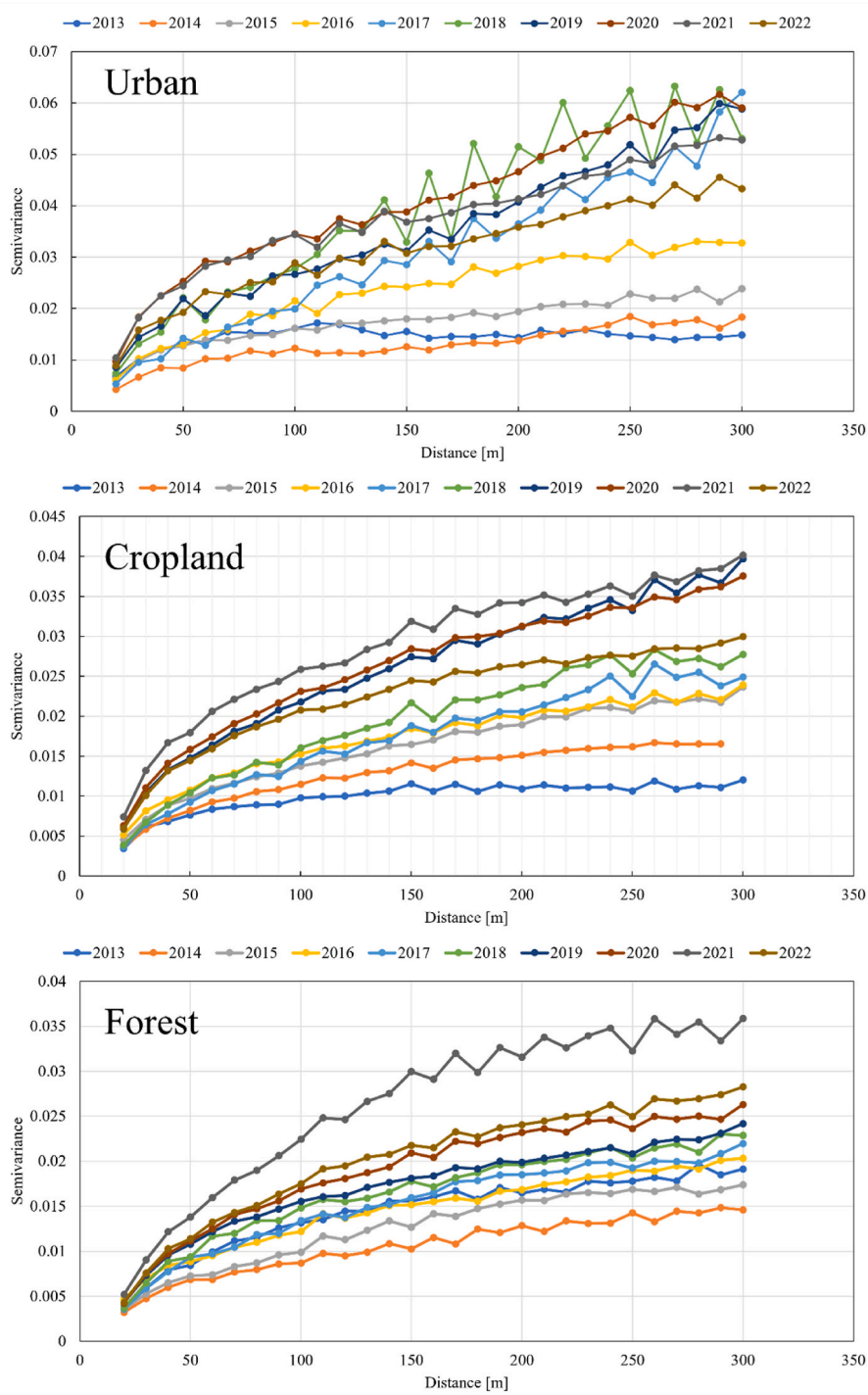

Fig. 4. The variogram of air dose rates for each land use during 2013–2022 in the evacuation area.

variogram of the air dose rates for each land use during 2013–2022 inside and outside the evacuation areas (also, Supplementary Fig. S5 shows the variogram and fitted curves of the air dose rates for forests in 2014, 2016, 2018, and 2020 inside the evacuation areas calculated using equation (3), for example). The walk survey data did not exist for 2011–2012; therefore, we used the variogram parameters of range, sill, and nugget obtained in 2013. The crucial point is that we can consider the heterogeneity in a small area because the variogram inside and outside the evacuation areas ranged under 300 m and 1 km, respectively. Generally, the relative magnitude of the variogram at a given distance increases first and then decreases at some years in all situations. The timing of the decrease depends on the situation, with a particularly early trend for urban areas and outside the evacuation areas.

From Fig. 4, the variograms in the air dose rates in the evacuation areas for each land use increased over the years. However, the semivariance of the variograms for urban areas decreased after 2020 and decreased for cropland and forest areas after 2021. However, from Fig. 5, the semivariance of the variograms in air dose rate outside the evacuation areas for urban areas increased from 2013 to 2015, then decreased over the years. The semivariance for cropland and forest areas increased over the years and decreased after 2019.

The semivariance of the variogram's increase could be caused by the changes in the heterogeneity of radiocesium distribution in the environment due to the contrast between decontaminated/un-

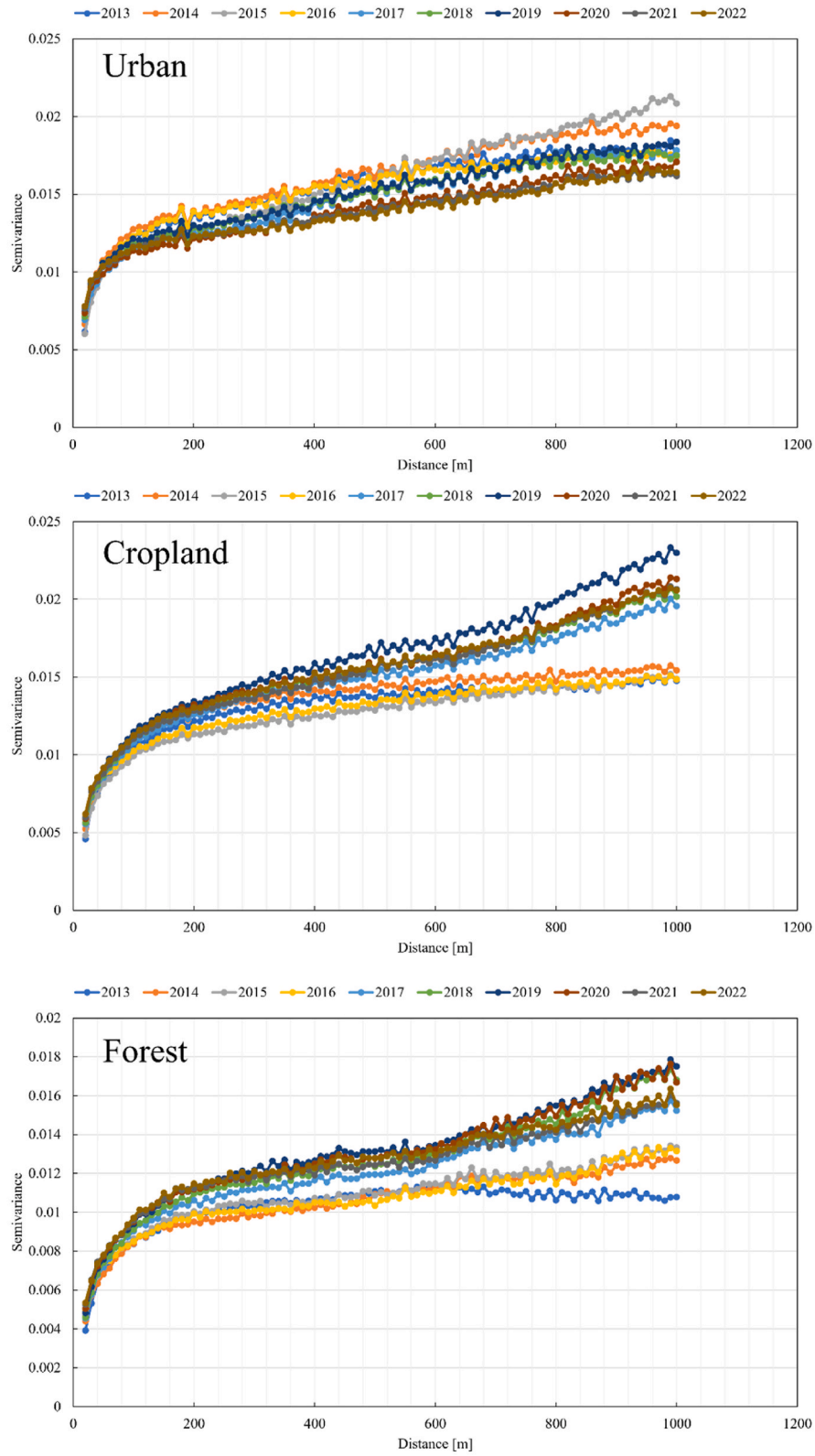

Fig. 5. The variogram of air dose rates for each land use during 2013–2022 outside the evacuation area.

decontaminated areas. On the other hand, the semivariance of the variogram's decrease could be caused by a reduced absolute value in air dose rates with year and a homogenization of the radiocesium distribution in the environment due to the weathering effect and human activity. Therefore, the variogram changes in the air dose rate could depend on the balance of increasing and decreasing factors. The air dose rate for urban areas decreased quickly because the radiocesium on the roads easily washes off (Yoshimura et al., 2017) and is removed by car driving (Saito et al., 2019; Andersson et al., 2002; Andoh et al., 2018b). However, air dose rate reduction for cropland and forest areas is slow

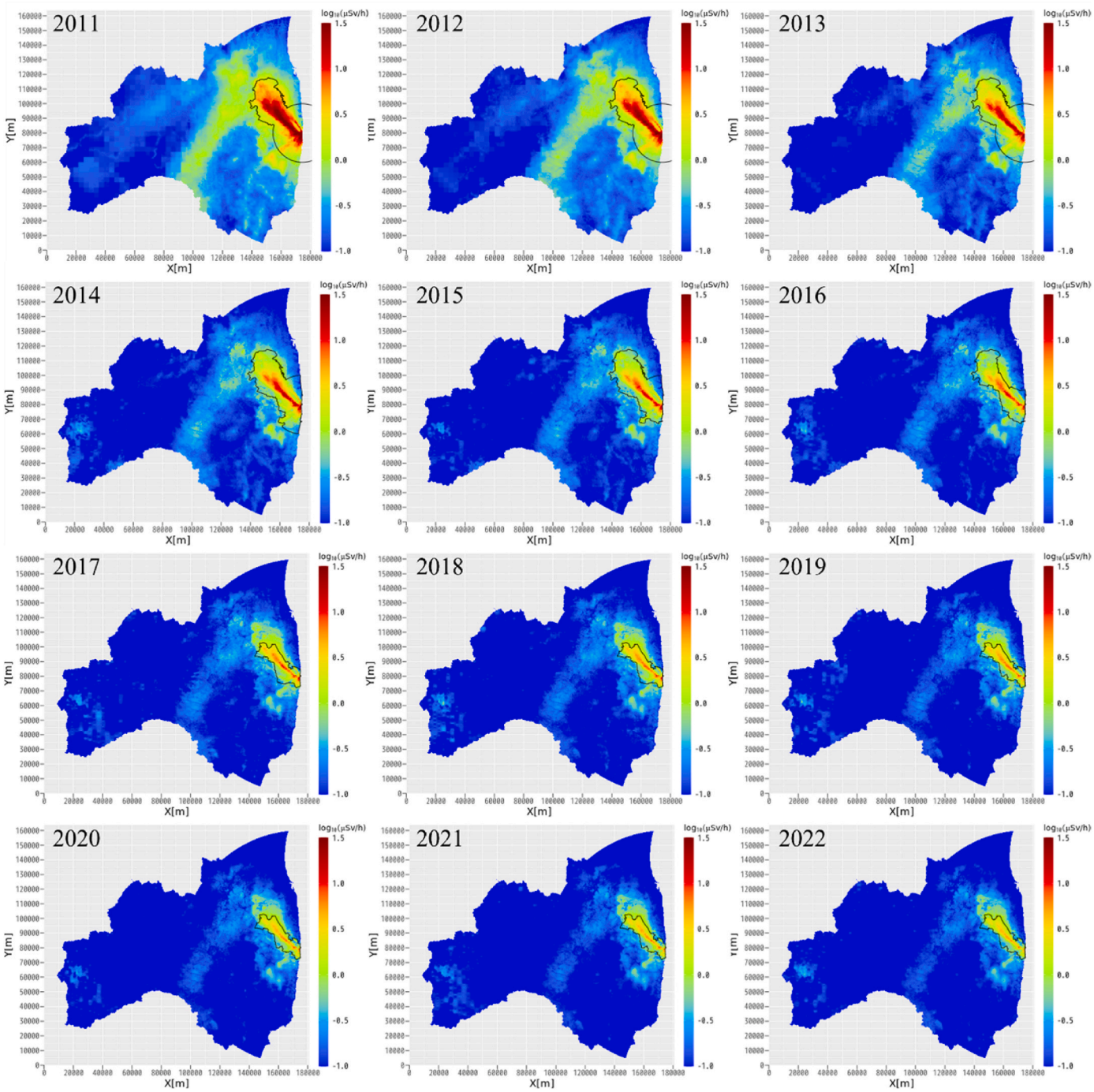

Fig. 6. Integrated maps of air dose rates over the 80 km radius of the Fukushima Daiichi Nuclear Power Plant (FDNPP) and the entire Fukushima Prefecture for 12 years.

because radiocesium penetration in the soil is slow (Imamura et al., 2017). Thus, the semivariance decrease rates by the weathering effect (wash-off and deeper migration in soil) are fast in urban areas and slow in croplafnd and forest areas. Furthermore, the radiocesium behavior caused by sediment erosion and deposition near the river channel (Sakuma et al., 2018) would not significantly affect the spatial air dose rates measured by walk surveys and fixed-location measurements because radiocesium behavior associated with sediment transport is limited to the vicinity of rivers.

Most planned decontamination activities inside and outside evacuation areas were completed around 2023 and 2018, respectively (Ministry of the Environment, 2024). Fr om this viewpoint, the impact of decontamination activities in the evacuation areas could be more significant than the impact of weathering and human activities. Therefore, the semivariance of the variogram in urban areas increased until approximately 2020 and then decreased, whereas in cropland and forest areas, it increased until approximately 2021 and then decreased (Fig. 4). Since the decontamination activities outside the evacuation areas have been completed earlier than in the evacuation areas and the impact of human activities is greater, the semivariance of the variogram in urban areas increased until approximately 2015 and then decreased (Fig. 5). However, in cropland and forest areas, it increased until approximately 2019 and then decreased (Fig. 5).

Table 2
Integrated maps with the year over the 80 km radius of the FDNPP.

Year	Mean of a prior distribution [log (μSv/h)]	SD of a prior distribution [log (μSv/h)]	Mean of a posterior distribution [log (μSv/h)]	SD of a posterior distribution [log (μSv/h)]
2011	0.108	0.120	0.137	0.111
2012	−0.063	0.120	−0.001	0.110
2013	−0.238	0.119	−0.187	0.109
2014	−0.367	0.118	−0.317	0.107
2015	−0.470	0.121	−0.421	0.109
2016	−0.554	0.119	−0.487	0.109
2017	−0.586	0.125	−0.571	0.110
2018	−0.629	0.128	−0.623	0.112
2019	−0.692	0.132	−0.635	0.115
2020	−0.742	0.131	−0.726	0.115
2021	−0.759	0.131	−0.735	0.116
2022	−0.791	0.130	−0.771	0.115

SD: standard deviation.

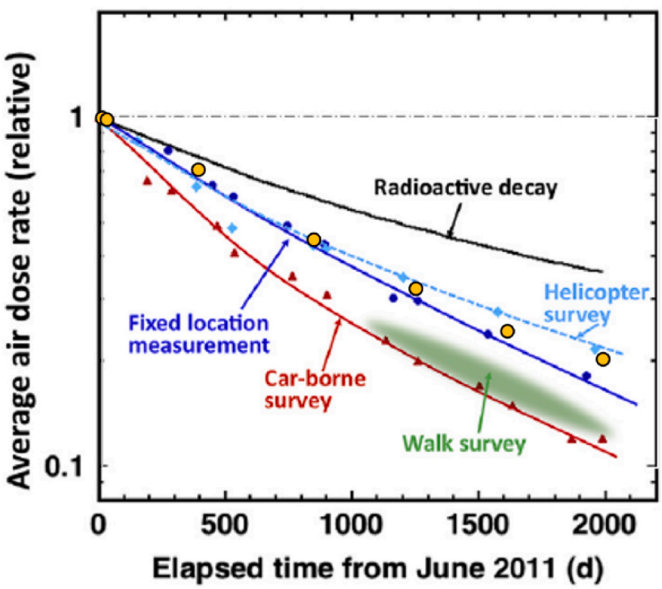

Fig. 7. Overall decay curves between each survey (Saito et al., 2019) and integrated map. Orange circles show the average air dose rate (relative) in the integrated map. (For interpretation of the references to colour in this figure legend, the reader is referred to the Web version of this article.)

3.3. Visualization of air dose rates over 80 km and Fukushima Prefecture during 2011–2022

Fig. 6 shows the integrated maps of air dose rates over the 80 km radius of the FDNPP and the entire Fukushima Prefecture during 2011–2022 (all data can be downloaded at https://doi.org/10.60427/0002000022). Table 2 shows the mean and standard deviations of the integrated maps over the 80 km radius of the FDNPP for each year. Fig. 7 compares the air dose rate trend based on the integrated maps to the trends obtained from different survey methods reported by Saito et al. (2019). We normalized the average air dose rate each year to that on June 14, 2011, to compare the results from Saito et al. (2019). The decreasing rates of each survey and integrated map were faster than that of radioactive decay due to the weathering and decontamination effects. Compared to other survey results, the integrated map with the most realistic air dose rate data showed a decreasing curve between the airborne survey and fixed-location measurements (Fig. 7). According to Saito et al. (2019), within an 80 km radius of the FDNPP, 70% of radiocesium was deposited in forest, 25% on farmland (including paddies), and 5% in urban areas. Thus, the integrated maps of air dose rates over

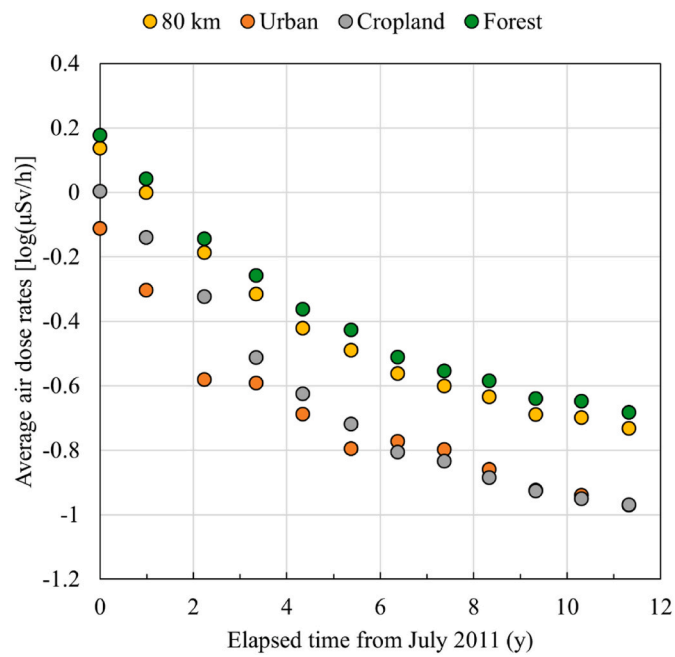

Fig. 8. Time series of the air dose rate for each land use within an 80 km radius of the Fukushima Daiichi Nuclear Power Plant (FDNPP) and the overall average within 80 km of the FDNPP by the integrated map.

an 80 km radius of the FDNPP showed the decreasing curve between the airborne survey and fixed-location measurement due to the large contribution of the highly contaminated forested areas. However, the strong point of the integrated map is that it can accurately represent air dose rates over the entire area with a 50 m resolution while capturing local variations such as those obtained from walk and car-borne surveys.

Fig. 8 shows the time series in air dose rates for each land use within the 80 km radius of the FDNPP and for the average within 80 km of the FDNPP by the integrated map. The air dose rates in forests have the highest values of the three land uses, followed by cropland and urban areas, although cropland and urban areas have had similar values since 2017. The high average air dose rates in forests from the beginning of the accident resulted from the high forest area being highly contaminated. For all land uses, the decreasing rates are faster in the early stages after the accident due to physical decay. Furthermore, the decreasing rates in the early stage were faster in the order of urban areas, croplands, and forests, coinciding with the results obtained from the car-borne survey data (Andoh et al., 2015, 2018b).

Previous studies have used walk surveys as a prior distribution, which underestimated the air dose rates in forests (Wainwright et al., 2019). This study added fixed-location measurement data, including forested areas, which was expected to improve the reproducibility of the air dose rates in forested areas. Supplementary Fig. S6 confirms that adding the fixed-location measurement data, including forested areas, improved the underestimation trend, and the method used in this study improved the reproducibility of the integrated maps. The mean squared errors of log-transformed air dose rates with and without data in forest areas were estimated at 0.331 (±0.104) and 1.074 (±0.154) μSv/h for designated evacuation areas until 2013 and 1.067 (±0.096) and 1.074 (±0.154) μSv/h for recreational forest areas.

The impact of changes in evacuation areas also requires attention. In this study, we confirmed the impact of changes in the evacuation areas for 2016 and 2017, when the variograms changed significantly in cropland and forest areas outside the evacuation areas (Fig. 5). Specifically, the variograms were calculated for the case where the 2017 evacuation areas were applied to the 2016 survey data, and the 2016 evacuation areas were applied to the 2017 survey data. Consequently, the variograms for the former case did not differ from those obtained

when applying the 2016 evacuation areas to the 2017 survey data; however, a different variogram was obtained (the data were not shown). In other words, the change in the evacuation areas might affect the variogram, but the large change in the 2016–2017 variogram might be due to different factors (ex., the period of the large-scale decontamination).

4. Conclusions

We expanded Wainwright et al.'s (2017) method using domain decomposition and created integrated maps of air dose rates over an 80 km radius of the FDNPP and the entire Fukushima Prefecture from 2011 to 2022. In this study, adding fixed-location measurements, including forested areas, to the airborne, car-borne, and walk survey data used in Wainwright et al. (2017, 2019) enabled us to create integrated maps in 2011 and 2012, when no walk survey data existed. The air dose rates obtained by different survey methods were similar in 2011. However, in 2020, the relationship slopes between them were 1.3 (airborne), 0.6 (walk), and 0.5 (car-borne) when the fixed-location measurements were set at 1. The temporal changes in the variograms indicate the heterogeneity of radiocesium due to decontamination activities and the homogeneity of radiocesium due to surface runoff on the roads, penetration in soil, and human activities.

Furthermore, the change tendency differed between land use and inside and outside the evacuation zone. The results indicate that the increase and decrease in heterogeneity occurred earlier outside the evacuation zone, where decontamination was conducted, and more active human activity was involved. We created a broad, time-series-integrated map for July 2011–2022, which reproduced the air dose rates in forested areas that had been underestimated in previous studies. The decreasing rate in the integrated map was considered the most representative of the overall decreasing rate, which was between fixed-location measurements and airborne surveys. Detailed exposure assessment using the integrated map is expected in the future.

CRediT authorship contribution statement

Kazuyuki Sakuma: Writing – original draft, Visualization, Methodology, Investigation, Formal analysis, Data curation. **Hiroshi Kurikami:** Writing – review & editing, Validation, Supervision, Methodology, Investigation, Formal analysis, Conceptualization. **Haruko Wainwright:** Writing – review & editing, Methodology, Conceptualization. **Soichiro Tanimori:** Visualization, Validation, Software, Methodology, Investigation, Data curation. **Fumiya Nagao:** Project administration. **Kotaro Ochi:** Writing – review & editing, Methodology. **Yukihisa Sanada:** Supervision, Project administration, Methodology, Funding acquisition, Conceptualization. **Kimiaki Saito:** Writing – review & editing, Supervision, Methodology, Conceptualization.

Declaration of competing interest

The authors declare that they have no known competing financial interests or personal relationships that could have appeared to influence the work reported in this paper.

Acknowledgments

This study was performed as part of the mapping project and the airborne survey project funded by the Ministry of Education, Culture, Sports, Science, and Technology (MEXT) and the Nuclear Regulation Authority, Japan. We thank members of the Sector of Fukushima Research and Development and the Center for Computational Science & e-Systems for their support in this research.

Appendix A. Supplementary data

Supplementary data to this article can be found online at https://doi.org/10.1016/j.jenvrad.2024.107554.

Data availability

Data will be made available on request.

References

Andersson, K.G., Roed, J., Fogh, C.L., 2002. Weathering of radiocaesium contamination on urban streets, walls and roofs. J. Environ. Radioact. 62, 49–60.

Andoh, A.A., Koarashi, J., Takeuchi, E., Tsuduki, K., Nishimura, S., Matsunaga, T., 2015. Catchment-scale distribution of radiocesium air dose rate in a mountainous deciduous forest and its relation to topography. J. Environ. Radioact. 147, 1–7.

Andoh, M., Nakahara, Y., Tsuda, S., Yoshida, T., Matsuda, N., Takahashi, F., Mikami, S., Kinouchi, N., Sato, T., Tanigaki, M., Takamiya, K., Sato, N., Okumura, R., Uchihori, Y., Saito, K., 2015. Measurement of air dose rates in wide area around the Fukushima Daiichi nuclear power plant through a series of car-borne surveys. J. Environ. Radioact. 139, 266–280.

Andoh, M., Mikami, S., Tsuda, S., Yoshida, T., Matsuda, N., Saito, K., 2018a. Measurement of air dose rates by walk survey around the Fukushima Dai-ichi Nuclear Power Plant using KURAMA-II until 2016. J. Environ. Radioact. 190–191, 111–121.

Andoh, M., Mikami, S., Tsuda, S., Yoshida, T., Matsuda, N., Saito, K., 2018b. Decreasing trend of ambient dose equivalent rates over a wide area in eastern Japan until 2016 evaluated by car-borne surveys using KURAMA Systems. J. Environ. Radioact. 192, 385–398.

Fukushima prefecture. Available at: https://www.pref.fukushima.lg.jp/site/portal/ps-monitoring-mesh-syousai.html–. (Accessed 4 August 2023).

Imamura, N., Komatsu, M., Ohashi, S., Hashimoto, S., Kajimoto, T., Kaneko, S., Takano, T., 2017. Temporal changes in the radiocesium distribution in forests over the five years after the Fukushima Daiichi Nuclear Power Plant accident. Sci. Rep. 7, 8179.

Japan Aerospace Exploration Agency (JAXA), 2022. ALOS data. Available at: https://www.eorc.jaxa.jp/ALOS/en/dataset/lulc_e.htm. (Accessed 19 February 2024).

Kato, H., Onda, Y., Gao, X., Sanada, Y., Saito, K., 2019. Reconstruction of a Fukushima accident-derived radiocesium fallout map for environmental transfer studies. J. Environ. Radioact. 210, 105996.

Ministry of Agriculture Forestry and Fisheries (MAFF). Available at https://www.rinya.maff.go.jp/kanto/seibi/jyosensennta/chousakekka01.html (Accessed19 February 2024) (in Japanese).

Ministry of economy, trade and industry (METI). Available at: https://www.meti.go.jp/earthquake/nuclear/release.html#monitoring–. (Accessed 19 February 2024) (in Japanese).

Ministry of the Environment, 2024. Available at: http://josen.env.go.jp/en/. (Accessed 19 January 2024).

Mikami, S., Maeyama, T., Hoshide, Y., Sakamoto, R., Sato, S., Okuda, N., Demongeot, S., Gurriaran, R., Uwamino, Y., Kato, H., Fujiwara, M., Sato, T., Takemiya, H., Saito, K., 2015a. Spatial distributions of radionuclides deposited onto ground soil around the Fukushima Dai-ichi Nuclear Power Plant and their temporal change until December 2012. J. Environ. Radioact. 139, 320–343.

Mikami, S., Maeyama, T., Hoshide, Y., Sakamoto, R., Sato, S., Okuda, N., Sato, T., Takemiya, H., Saito, K., 2015b. The air dose rate around the Fukushima Dai-ichi Nuclear Power Plant: its spatial characteristics and temporal changes until December 2012. J. Environ. Radioact. 139, 250–259, 2015.

Mikami, S., Tanaka, T., Matsuda, H., Sato, S., Hoshide, Y., Okuda, N., Suzuki, T., Sakamoto, R., Andoh, M., Saito, K., 2019. The deposition densities of radiocesium and the air dose rates in undisturbed fields around the Fukushima Dai-ichi Nuclear Power Plant; their temporal changes for five years after the accident. J. Environ. Radioact. 210, 105941.

Ribeiro, P.J., Diggle, P.J., 2001. geoR: a package for geostatistical analysis. ISSN R-NEWS 1 (2), 1609–3631, 15-18.

Saito, K., Onda, Y., 2015. Outline of the national mapping projects implemented after the Fukushima accident. J. Environ. Radioact. 139, 240–249.

Saito, K., Mikami, S., Andoh, M., Matsuda, N., Kinase, S., Tsuda, S., Yoshida, T., Sato, T., Seki, A., Yamamoto, H., Sanada, Y., Wainwright, H.M., Takemiya, H., 2019. Summary of temporal changes in air dose rates and radionuclide deposition densities in the 80 km zone over five years after the Fukushima Nuclear Power Plant accident. J. Environ. Radioact. 210, 105878.

Sanada, Y., Sugira, T., Nishizawa, Y., Kondo, A., Torii, T., 2014. The aerial radiation monitoring in Japan after the Fukushima Daiichi nuclear power plant accident. J. Prog. In Nucl. Sci. Technol. 4, 76–80.

Sanada, Y., Urabe, Y., Sasaki, M., Ochi, K., Torii, T., 2018. Evaluation of ecological halflife of dose rate based on airborne radiation monitoring following the Fukushima Daiichi nuclear plant accident. J. Environ. Radioact. 192, 417–425.

Sanada, Y., Ishida, M., Yoshimura, K., Mikami, S., 2019. Comparison of dose rates from four surveys around the Fukushima Daiichi nuclear power plant for location factor evaluation. J. Radiation Protection and Research 46 (4), 184–193.

Sakuma, K., Malins, A., Funaki, H., Kurikami, H., Niizato, T., Nakanishi, T., Mori, K., Tada, K., Kobayashi, T., Kitamura, A., Hosomi, M., 2018. Evaluation of sediment and ^{137}Cs redistribution in the Oginosawa River catchment near the Fukushima Dai-ichi

Nuclear Power Plant using integrated watershed modeling. J. Environ. Radioact. 182, 44–51.
Sato, T., Andoh, M., Sato, M., Saito, K., 2019. External dose evaluation based on detailed air dose rate measurements in living environments. J. Environ. Radioact. 210, 105973. https://doi.org/10.1016/j.jenvrad.2019.05.005, 2019.
Takeishi, M., Shibamichi, M., Malins, A., Kurikami, H., Murakami, M., Saegusa, J., Yoneya, M., 2017. Using two detectors concurrently to monitor ambient dose equivalent rates in vehicle surveys of radiocesium contaminated land. J. Environ. Radioact. 177, 1–12.
Tanigaki, M., Okumura, R., Takamiya, K., et al., 2015. Development of KURAMA-II and its operation in Fukushima. Nucl. Instrum. Methods Phys. Res. 781, 57–64.
Tsuda, S., Yushida, T., Tsutsumi, M., Saito, K., 2015. Characteristics and verification of a car-borne survey system for dose rates in air: KURAMA-II. J. Environ. Radioact. 139, 260–265.
Wainwright, H.M., Seki, A., Chen, J., Saito, K., 2017. A multiscale Bayesian data integration approach for mapping air dose rates around the Fukushima Daiichi Nuclear Power Plant. J. Environ. Radioact. 167, 62–69.
Wainwright, H.M., Seki, A., Mikami, S., Saito, K., 2019. Characterizing regional-scale temporal evolution of air dose rates after the Fukushima Daiichi Nuclear Power Plant. J. Environ. Radioact. 210, 213–222.
Wong, D., 2017. Interpolation: inverse-distance weighting. In: International Encyclopedia of Geography: People, the Earth, Environment and Technology. Wiley Online Library.
Yoshimura, K., Saito, K., Fujiwara, K., 2017. Distribution of ^{137}Cs on components in urban area four years after the Fukushima Dai-ichi Nuclear Power Plant accident. J. Environ. Radioact. 178–179, 48–54.